



Development of Kriging-approximation simulated annealing optimization algorithm for parameters calibration of porous media flow model

Ming-Che Hu¹ · Chia-Hui Shen¹ · Shao-Yiu Hsu¹ · Hwa-Lung Yu¹ · Krzysztof Lamorski² · Cezary Sławiński²

Published online: 18 January 2019
© Springer-Verlag GmbH Germany, part of Springer Nature 2019

Abstract

This research proposes an innovative Kriging-approximation simulated annealing (KASA) optimization algorithm to increase optimization efficiency and reduce the computation time for the parameter calibration of simulation model. The newly developed KASA optimization algorithm utilizes the simulated annealing algorithm to search the global optimum; meanwhile, Kriging approximation, a statistical estimation method, is incorporated with simulated annealing to interpolate unknown objective values in solution spaces. Furthermore, this research establishes a network-based porous media flow simulation (NET-PFS) model and then KASA is applied in the calibration of the NET-PFS representative pore network. NET-PFS is a pore network based model constructing a representative pore network to approximate soil characteristics and pore geometry with limited access to pore-scale imaging processes. NET-PFS is applied to estimate the permeability of a sand-packing porous media. NET-PFS establishes a framework for simplifying the pore network but remaining the same hydraulic conductivity and the flow status of pore networks with limited information about the pore structure. In the case study, a quartz sand-packing porous media is scanned by X-ray micro computed tomography. The NET-PFS model is applied to estimate the hydraulic conductivity and flow velocity distribution from the original pore network. The results demonstrate the proposed KASA algorithm effectively calibrated the NET-PFS model; in addition, a representative pore network and the determined flow status in the pore network is presented by NET-PFS.

Keywords Kriging approximation · Simulated annealing · Network-based porous media flow · Representative pore network

List of symbols

Indices

i Unobserved points, $i = 1, 2, 3, \dots, m$
 $j1, j2, k$ Observed points, $j1, j2, k = 1, 2, 3, \dots, n$
 $r1, r2$ Pores, $r1, r2 = 1, 2, 3, \dots, q1$
 $r3$ Inner pores, $r3 = 1, 2, 3, \dots, q3$
 $r4$ Boundary pores, $r4 = 1, 2, 3, \dots, q4$

Parameters and variables

$a_{r1,r2}$ Length of the arc between pores $j1$ and $j2$
 $ar_{r1,r2}$ Diameter of the arc between pores $j1$ and $j2$
 dv Dynamic viscosity
 $d_{j1,j2}$ Distance between points $j1$ and $j2$
 obj_{new} New objective value
 $obj_{current}$ Current objective value
 p Number of simulated annealing iterations
 pr_{r4} Given node pressure at node $r4$ of the NET-PFS model
 qa Number of arcs in the pore network
 $q1$ Number of pores in the pore network
 $q3$ Number of inner pores in the pore network
 $q4$ Number of boundary pores in the pore network
 $temp$ Temperature of the simulated annealing algorithm
 tk Computational time of the Kriging approximation for the NET-PFS model

✉ Shao-Yiu Hsu
syhsu@ntu.edu.tw

¹ Department of Bioenvironmental Systems Engineering, National Taiwan University, No. 1, Sec. 4, Roosevelt Road, Taipei 10617, Taiwan

² Institute of Agrophysics, Polish Academy of Sciences, Doświadczalna 4, 20-290 Lublin, Poland

t_n	Computational time of the NET-PFS model
v_i^E	Kriging estimation of a random variable at unobserved point i
v_i^T	Realization of a random variable at unobserved point i
v_{j1}	Realization of a random variable at observed point $j1$
w_{j1}	Kriging weight at point $j1$
$xf_{r1,r2}$	Arc flow from nodes $r1$ to $r2$ of the NET-PFS model
$x_{p_{r1}}$	Node pressure at node $r1$ of the NET-PFS model
$x_{p_{in}}$	Pore pressure at the inlet boundary
$x_{p_{out}}$	Pore pressure at the outlet boundary
z	Random variable with a uniform distribution in the interval of $[0,1]$
$\gamma(d_{j1,j2})$	Semivariogram function of distance $d_{j1,j2}$
λ	Lagrange multiplier
μ	Expected values of the random variables
σ^2	Variance of the random variables

Functions

COV	Covariance function
ERROR _{i}	Estimation error at unobserved point i
EXP	Expected value
EXPO	Exponential function
LAGR _{i}	Lagrange function at unobserved point i
Q_m	Total flow rate
VAR	Variance function

1 Introduction

This study proposes an innovative Kriging-approximation simulated annealing (KASA) algorithm. The KASA algorithm incorporates simulated annealing with Kriging approximation to save computational time of iterative objective function evaluation. The proposed KASA algorithm applies Kriging approximation to interpolate the objective value in the solution space rather than to estimate random variables in physical space. The simulated annealing algorithm is often used for water resources management, model calibration, decision making, etc. (Bechler et al. 2013; Cao and Ye 2013; Cieniawski et al. 1995; Dougherty and Marryott 1991; Jiang et al. 2018; Marryott et al. 1993). It is a heuristic optimization algorithm that seeks the global optimum by simulating the cooling process of heated metals. The algorithm evaluates a new solution if the new solution has a better objective value than the current solution. To jump out of the local optimum, the algorithm still accepts the new solution on the basis of the acceptance probability, if the new solution has a worse objective value than the current solution. The

acceptance probability is negatively proportional to the metal temperature. Since the temperature decreases during the cooling process, the acceptance probability function decreases and it leads to the convergence of the global optimum. Most importantly, the newly proposed KASA algorithm utilizes Kriging approximation, a statistical interpolation method, to reduce the evaluation time of the objective function for simulated annealing search. The Kriging method is often used for statistical interpolation in hydrology, atmospheric processes, geophysics, etc. (de Lavenne et al. 2016; Verdin et al. 2015; Laaha et al. 2014; Oliver and Webster 1990; Yeh 1986). It is a spatial statistical estimation method that can estimate an unknown variable at a given point by calculating the weighted average of known values at given points in the neighborhood. The method is also a linear interpolation method that provides an optimal and unbiased estimation of unknown random variables.

In this research, a case study of the KASA optimization algorithm was conducted for parameters calibration of the representative pore network. Then, a porous media flow model was formulated to analyze the flow velocity and pore pressure distribution in a packed quartz sand medium. Traditionally, owing to the complexity of the pore geometry, the flows in porous media were treated macroscopically and are described by Darcy's law. The uncertainty and the heterogeneity of the subsurface geological structure is one of the key issues of flow and mass transportation simulation of the groundwater contamination. In the last three decades, pore-scale modeling has developed rapidly from a pure scientific-oriented method for studying fluid displacement to a predictive tool used in the oil industry (Blunt et al. 2013). The rapid development is based on the more sophisticated construction of models for the pore geometry and on the predictive power for the dynamics of multiphase flow (Blunt et al. 2002; Keehm et al. 2004; Oren et al. 1998; Piri and Blunt 2005; Raeini et al. 2015; Steefel et al. 2015). Continuum and discrete approaches are commonly used to compute the fluid properties in the pore space. The first is to discretize the voids using a grid derived from a binarized three-dimensional (3D) pore-scale image and then compute the flow and transport on this grid. Nevertheless, most of the existing techniques are computationally demanding. Network modeling is an alternative method, which first extracts a representative network on the basis of the binarized pore-scale image (Blunt et al. 2013). Then, the flow and transport are computed, usually semi-analytically, through this network. The computational demand of the pore-network model is much lower than that of the first method. The abovementioned pore-scale simulation can provide not only the details of the flow behaviors but also the pore structure properties or the soil characteristics, i.e., the parameters of the water retention curves,

which, traditionally, can only be obtained through time-consuming laboratory experiments. An overview of these imaging techniques applied to the earth sciences is provided by Ketcham and Carlson (2001). For example, if a 3D image is available (experimental or synthetically generated), pore networks can be constructed directly from this image, assuming what is considered to be a pore and what to be a throat between pores. (Miao et al. 2017) used neural networks to predict the dimensionless hydraulic conductance based on the circularity, convexity and elongation of each pore element. However, binarizing the pore imaging and extracting the pore network are also computationally demanding (Xiong et al. 2016). Abovementioned methods are still limited to samples with centimeter scales, which might have contained more than 10,000 pores and pore throats (Dong and Blunt 2009). The need for up-scaling from the typically small imaged volume to larger domains leads to the need for construction of statistically representative networks.

Statistical methods have been used to reconstruct the equivalent pore-network structure (Xiong et al. 2016). Yeong and Torquato (1998) developed a stochastic method based on simulated annealing to minimize the objective function and they obtained the correct porosity by moving pore space voxels around. Okabe and Blunt (2004) developed a multi-point statistical method aiming to construct the 3D representative pore network from the measured 2D images of the porous media with similar pore structure statistics. Bryant and co-workers pioneered the use of geologically realistic networks based on random close packing of equally-sized spheres (Bryant and Blunt 1992; Bryant et al. 1993a, b). (Bakke and Oren 1997; Lerdahl et al. 2000; Øren and Bakke 2002; Oren et al. 1998) simulated the packing of spheres of different size based on the grain size distribution from analysis of thin sections of the rock of interest. The works of Pillotti, and Coelho and co-workers have demonstrated a method to simulate the deposition of grains of non-spherical shapes, in particular, enabling the reconstruction technique to be applied more generally (Coelho et al. 1997; Pillotti 2000). Also, in order to reduce the computational time, reconstructing a representative pore network based on statistically information extracted from the pore-scale image to keep the pore-scale information is of interest to the up-scaling work.

Adding pore structure information based on pore-scale imaging into the statistical method might enhance the reconstruction process. Therefore, we proposed a hybrid method combining a heuristic/statistical method and limited information provided by direct mapping method to reconstruct an equivalent pore-network incorporating information of real pore structure. This study applied a network-based porous media flow simulation (NET-PFS) model to explore pore geometry and analyze flows in

porous media. The model is capable of simulating a representative pore network and analyzing the flow status with limited information about the pore structure.

However, constructing a representative pore network by parameter calibration is computationally demanding. An effective search algorithm is therefore needed. Hence, the newly proposed KASA algorithm was developed to calibrate the pore network of the target sample for the NET-PFS model.

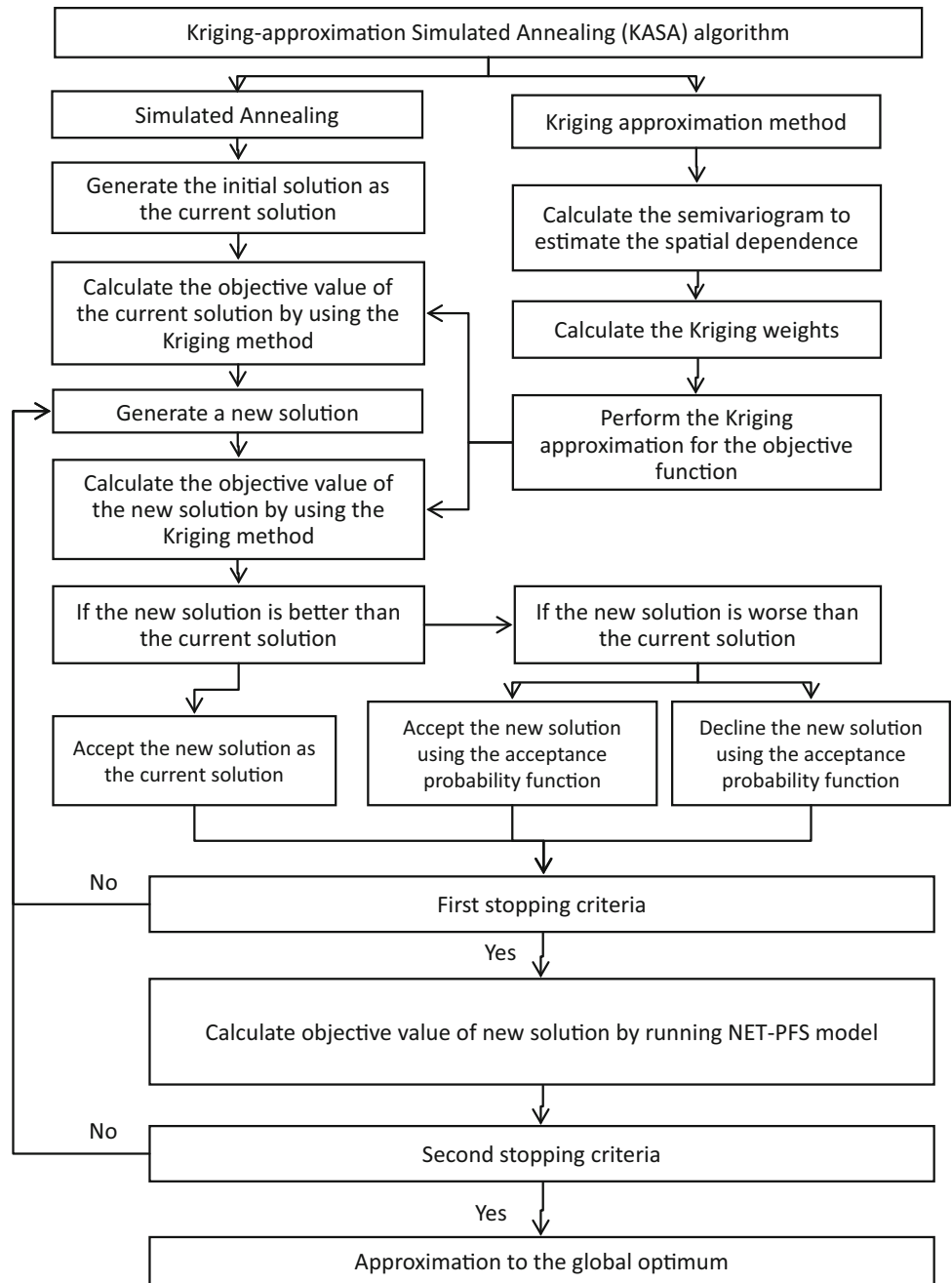
This study makes three major contributions. First, an innovative KASA algorithm based on simulated annealing and Kriging approximation was developed to increase optimization searching efficiency. Second, this research built a representative pore network with limited information about the soil samples. A framework combining pore network simulation and KASA algorithm was developed to generate the equivalent pore network based on the pore-structure statistical information. Third, this study successfully conducted a case study of the KASA algorithm for calibrating the parameters of the equivalent pore network of a sand packing porous medium for NET-PFS model. The rest of the paper is organized as follows. The methodology of the KASA algorithm is developed in Sect. 2. An application of the KASA algorithm for calibrating the NET-PFS model with a packed quartz sand medium is demonstrated in Sect. 3. Results and discussion are presented in Sect. 4. Finally, the conclusion is presented in Sect. 5.

2 The KASA algorithm

The newly developed KASA algorithm is an efficient optimization algorithm especially designed to optimize problems with a complicated objective function. The KASA algorithm combines simulated annealing with Kriging interpolating approximation. More specifically, the KASA search procedures mainly follow the simulated annealing algorithm; in addition, the Kriging approximation method is utilized to approximate the evaluation of the complicated objective function during the running of the KASA algorithm. The detailed KASA algorithm is derived in the following, and a flowchart of the algorithm is proposed in Fig. 1.

The search procedure of the KASA algorithm is similar to that of simulated annealing. The simulated annealing algorithm is a heuristic optimization algorithm that simulates the cooling process of heated metals. In the cooling process, while the metal temperature decreases, the metal structure gradually converges to a stable condition. Similarly, this optimization algorithm approaches the global optimum step by step with a probabilistic technique. At each iteration of the algorithm, the KASA algorithm takes the steps from the current solution to the new solution when the new solution has a better objective value than the

Fig. 1 Flowchart of the Kriging-approximation simulated annealing (KASA) algorithm



current solution. Suppose the problem seeks a minimal objective value. The new solution is better if it has a smaller objective value, i.e., $obj_{new} \leq obj_{current}$; it would then be accepted without any exception. In contrast, if the new solution is worse, i.e., $obj_{new} > obj_{current}$, the algorithm accepts the new solution on the basis of a probability distribution function that is negatively proportional to the metal temperature. The algorithm generates a random number z with a uniform distribution in the interval of $[0, 1]$. The new solution is accepted only if z is less than or equal to an exponential function

$EXPO[-(obj_{new} - obj_{current})/temp]$ in Eq. (1); otherwise, the new solution is rejected when Eq. (2) holds.

$$obj_{new} \text{ is accepted} \quad (1)$$

$$\text{if } z \leq EXPO[-(obj_{new} - obj_{current})/temp]$$

$$obj_{new} \text{ is rejected} \quad (2)$$

$$\text{if } z > EXPO[-(obj_{new} - obj_{current})/temp]$$

Notice that the evaluation of the complicated objective function could be time consuming for a large-scale and complex model. Therefore, the newly developed KASA algorithm estimates the objective value by using Kriging

approximation. The more approximation is used, the greater is the computational efficiency provided by the KASA algorithm. Kriging is a statistical method that is used for spatial interpolation; it is used to predict the best linear unbiased estimation (BLUE) of unknown random variables. It estimates an unknown variable at a given point i by calculating the weighted average of known values at given points $j1$ in the neighborhood where $i = 1, 2, 3, \dots, m$ and $j1 = 1, 2, 3, \dots, n$. v_i^T and v_{j1} are the realization of random variables at point i and point $j1$, respectively. Suppose v_i^T and v_{j1} have the same expected values μ and the same variance σ^2 . The estimation v_i^E of random variable v_i^T at point i can be approximated by the weighted average of other known values, i.e. $v_i^E = \sum_{j1} [w_{j1} \times v_{j1}]$. Then expected estimation of v_i^T is unbiased as long as $\sum_{j1} [w_{j1}] = 1$. Furthermore, the expected square error $EXP[(v_i^E - v_i^T)^2]$ is computed in Eq. (3). To find the minimal expected square error, we need to minimize the Lagrange objective function $LAGR_i$ in Eq. (4). Hence, the partial derivatives of $LAGR_i$ with respect to decision variables w_k and λ should be equal to zero. The optimal weight w_{j1} and the optimal Lagrange multiplier λ are determined to minimize the expected square error of the Kriging method. The Kriging method uses a semivariogram function to estimate the spatial dependence among points. The semivariogram $\gamma(d_{j1,j2})$ is defined as half of the expected square difference between two field values at points $j1$ and $j2$. Notice that the semivariogram is a function that depends only on the distance between samples. Since covariance $COV[v_{j1}, v_{j2}]$ is equal to $\mu^2 - \gamma(d_{j1,j2})$, the optimality conditions becomes Eq. (5). Similarly, the Kriging weights and the Lagrange multiplier can be computed in matrix form of Eq. (6).

$$\begin{aligned}
 EXP[(ERROR_i)^2] &= EXP[(v_i^E - v_i^T)^2] = VAR[(v_i^E - v_i^T)] \\
 &= \sum_{j1,j2} [w_{j1} \times w_{j2} \times COV[v_{j1}, v_{j2}]] + \sigma^2 - 2 \\
 &\quad \times \sum_{j1} [w_{j1} \times COV[v_{j1}, v_i^T]] \quad \forall i
 \end{aligned}
 \tag{3}$$

$$\begin{aligned}
 MIN \quad LAGR_i &= \sum_{j1,j2} [w_{j1} \times w_{j2} \times COV[v_{j1}, v_{j2}]] + \sigma^2 \\
 &\quad - 2 \times \sum_{j1} [w_{j1} \times COV[v_{j1}, v_i^T]] \\
 &\quad + 2 \times \lambda \times \left(\sum_{j1} [w_{j1}] - 1 \right) \quad \forall i
 \end{aligned}
 \tag{4}$$

$$\sum_{j1} [w_{j1} \times \gamma(d_{k,j1})] - \lambda = \gamma(d_{k,i}) \quad \forall i, k \tag{5}$$

$$\begin{aligned}
 \begin{bmatrix} w_1 \\ w_2 \\ \dots \\ w_n \\ \lambda \end{bmatrix} &= \begin{bmatrix} \gamma(d_{1,1}) & \gamma(d_{1,2}) & \dots & \gamma(d_{1,n}) & -1 \\ \gamma(d_{2,1}) & \gamma(d_{2,2}) & \dots & \gamma(d_{2,n}) & -1 \\ \dots & \dots & \dots & \dots & \dots \\ \gamma(d_{n,1}) & \gamma(d_{n,2}) & \dots & \gamma(d_{n,n}) & -1 \\ 1 & 1 & \dots & 1 & 0 \end{bmatrix}^{-1} \\
 &\quad \times \begin{bmatrix} \gamma(d_{1,i}) \\ \gamma(d_{2,i}) \\ \dots \\ \gamma(d_{n,i}) \\ 1 \end{bmatrix} \quad \forall i
 \end{aligned}
 \tag{6}$$

This research incorporates a Kriging approximation method into the simulated annealing optimization algorithm. The KASA algorithm is constructed on the basis of the simulated annealing search mechanism, and, additionally, Kriging approximation is used to enhance the evaluation of the complicated objective function of the KASA algorithm. Since the calibration of the NET-PFS simulation model needs to be simulated for every optimization step, the KASA algorithm successfully increases the optimization efficiency by using the Kriging method to estimate the simulation results instead of running the NET-PFS model.

3 Case study

3.1 The NET-PFS model

The permeability of a porous medium can be estimated by simulate a steady-laminar single-phase flow in the porous medium. This research applied the NET-PFS model, which can be used to simulate a pore network and analyze porous media flows. Given the total pore volume and distribution of the pore size, the number, size, and location of pores are simulated by using Monte Carlo simulation. Then, a pore network is constructed by simulating a pore-throat connection. Assume the pore network has q_a arcs (pore throats) and q_1 nodes (pore spaces). Denote $x_{p_{r1}}$ as a node pressure at node $r1$, where index $r1 = 1, 2, 3, \dots, q_1$. Furthermore, $xf_{r1,r2}$ represents the arc flow delivered from $r1$ to $r2$; index $r2$ is also a node index that is the same as $r1$ ($r2 = 1, 2, 3, \dots, q_1$). In addition, nodes can be categorized into q_3 inner nodes and q_4 boundary nodes, i.e., $q_3 + q_4 = q_1$. In addition, the inner and boundary nodes are denoted by r_3 and r_4 , respectively, where $r_3 = 1, 2, 3, \dots, q_3$ and $r_4 = 1, 2, 3, \dots, q_4$.

The governing equations of the NET-PFS model contain mass balance equations and Poiseuille’s equations. The details of the physical meanings and mathematical derivations can be found in *Dullien (1992)*. The mass balance equation in Eq. (7) defines that, for each pore, the total inflow into the pore equals to total outflow from the pore.

$$\sum_{r1} x_{f_{r1,r3}} - \sum_{r1} x_{f_{r3,r1}} = 0 \quad \forall r3 = 1, 2, 3, \dots, q3 \quad (7)$$

Poiseuille’s equation in Eq. (10) is a physical law that describes an incompressible fluid flowing in a pipe with a constant cross section under a pressure drop. In Eq. (8), the pair-wise pressure equations that describe the arc flow rate $x_{f_{r1,r2}}$ from nodes $r1$ to $r2$ are proportional to the node pressure drop, $x_{p_{r1}} - x_{p_{r2}}$, of those two nodes (see Fig. 2).

$$x_{p_{r1}} - x_{p_{r2}} = \left[\frac{8\mu a l_{r1,r2} x_{f_{r1,r2}}}{\pi (a_{r1,r2})^4} \right] \quad (8)$$

$$\forall r1 = 1, 2, 3, \dots, q1; r2 = 1, 2, 3, \dots, q1$$

where μ is the viscosity of the fluid, a is the length of the arc, a is the radius of the arc.

A fixed pressure boundary condition is imposed on the boundary nodes as shown in Eq. (9).

$$x_{p_{r4}} = p_{r4} \quad \forall r4 = 1, 2, 3, \dots, q4 \quad (9)$$

The NET-PFS model solves the system of equations in Eqs. (7)–(9). The system of equations has $(q_a + q_3 + q_4)$ equations including q_3 mass balance equations, q_a Poiseuille’s equations, and q_4 boundary conditions. There are $q_a + q_3 + q_4$ unknown variables including q_a arc flow and $q_1 (= q_3 + q_4)$ node pressure variables. By solving the system of equations of the NET-PFS model, the flow rate and pore pressure of each arc and node of the porous media are determined.

The single pair pore network structure (see Fig. 2) can be extended to two or three-dimensional pore networks. As the dimension of the pore network increases, the number of the pores and throats exponentially increase as well as the size of the system of equations of the NET-PFS model. The NET-PFS model with m pores and n throats forms a system of equations with $n + m$ equations based on Eqs. (7)–(9). By solving the system of equations, the distributions of the

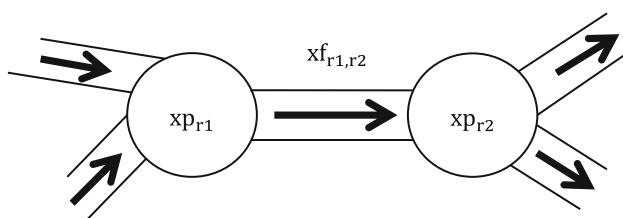


Fig. 2 Schematic of arc flow between two pores

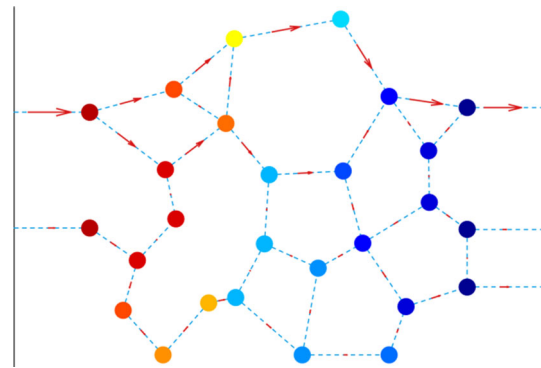


Fig. 3 Arc flows and pressure distribution in a pore network. The colors in the nodes indicate the fluid pressure from high (red) to low (blue), and the arrows show the flow directions and magnitudes

pressure in the pores and flow rate in the arc are determined as shown in the Fig. 3.

The hydraulic conductivity K of the pore network is found from Darcy’s law, $K = \frac{\mu Q L}{A \Delta \Phi}$, where μ is the viscosity of the fluid. The total flow rate through the network, Q_1 , is found by imposing a potential drop $\Delta \Phi$ across its length L , with A being the cross-sectional area of the model. Potential is defined as $\Phi = P - \rho gh$, where P is the pressure, ρ is the fluid density, g is the gravitational constant and h is the height above datum.

3.2 Pore-scale imaging and model parameters of a packed quartz sand medium

Since the number of control variables and equations of the NET-PFS model is large, we found that calibrating the model is computationally demanding. Hence, the case study used the NET-PFS model to simulate the flow rate, pore pressure, and permeability of a porous medium in a pore-network based on the pore structure of a porous medium with a sand-packing. The KASA algorithm was applied to seek the optimal indeterminate parameters of the NET-PFS model. The properties of the sand-packing soil were scanned and investigated by Computational X-ray microtomography (μ CT), and, then, the NET-PFS model simulated the porous media flow in the pore network.

μ CT analyses of sand samples were carried out using the GE Nanotom S device at the microtomography facility of the Institute of Agrophysics of the Polish Academy of Sciences (IAPAS) microtomography facility (Lamorski 2016). The voxel size achieved in the scan was $2 \mu\text{m}$. The parameters of the X-ray source were: accelerating voltage of 90 kV and cathode current of $120 \mu\text{A}$. A tungsten exit window was used for the X-ray generation. For the purpose of noise reduction, each of the two-dimensional (2D) images recorded during the scan was an average of 15

images. These images were used for the reconstruction of the 3D representation of the sample.

During the scan, the temperature in the μ CT chamber was stabilized, but the sample itself was heated by X-rays, which could cause thermal changes in the sample dimensions, which, in turn, could impact the reconstruction process in case of high-resolution scans. To overcome this problem, we performed a 30-min pre-scan prior to the main scan. During this pre-scan, the sample temperature was stabilized. After the pre-scan, the proper scan was started instantly.

After the scan, volume reconstruction and image processing were performed. 3D volume reconstruction was done using the DatosX 2.0 software. For the 3D image processing and visualization, the VG Studio Max software was used. The image processing procedure consisted of region-of-interest selection and 3D median filtering, with the kernel diameter equal to 3 pixels.

Figure 4 shows a 2D cross-sectional image of a packed quartz sand medium and a 2D pore network extracted from the selected section of the pore structure (red square). The reconstructed 3D image provides the basic information about the pore structure of the quartz sand medium; distributions of the radii of the pores (354 pores) and throats (443 throats) based on the maximum ball method (Al-Kharusi and Blunt 2007) follow gamma distribution as shown in Fig. 5. The dashed lines in Fig. 5 are the gamma distributions with the fitted parameters a and b .

The distributions of the radius of the pores and throats show that the pore structure of the packed quartz sand medium consists of pore spaces of a uniform radius with a few large pores/throats. However, the quality of the pore network of the quartz sand medium was highly dependent on the limitation of the resolution of the X-ray CT scanner and on the quality of the image. No pore throat/body with a radius smaller than $1\ \mu\text{m}$ was identified. The parameters of the model based on the limited information about the pore

structure were also extracted from the micro X-ray CT. The hydraulic conductivity was directly measured by Darcy's method.

Based on the probability distributions of the pore radius in Fig. 5, pore soil ratio, arc length, arc radius, and connectivity ratio among the pores of a real sand-packing porous medium, the pore network structures of the NET-PFS model were constructed by Monte Carlo simulation. A simulation of the size and location of the pore body is shown in Fig. 6. The connectivity of the nodes was simulated by the k nearest neighbor method. Furthermore, a pore network was simulated and is plotted in Fig. 7.

4 Results and discussion

In the case study, the NET-PFS model simulated the porous media flow in a $216\ \text{mm}^3$ ($= 6\ \text{mm} \times 6\ \text{mm} \times 6\ \text{mm}$) packed quartz sand medium. Figures 5 and 6 show an example of a randomly generated pore network for an arc radius of $r = 0.17$ (mm) and a connecting distance of $d = 1.2$ (mm). The generated pores were classified into three groups: isolated pores, boundary pores, and inner pores. In this example, there were 15 pores at the inlet boundary, 31 pores at the outlet boundary, and 303 inner pores. The volumes of the pores were generated on the basis of the pore volume distribution measured from the micro X-ray experiment. In the model, the constant pressure conditions at the inlet and outlet boundaries were $x_{p_{in}} = 10^4$ (Pa) and $x_{p_{out}} = 0$ (Pa), respectively; dynamic viscosity was $\nu = 1$ (Pa s). With the randomly generated pore network, we simulated the distributions of the water pressures at the pore bodies and the flow rates at the throats. In this case, the NET-PFS model generated a pore network model with 354 pores (303 inner pores and 46 boundary pores) and 443 pore throats. Accordingly, the model had 746 variables

Fig. 4 A two-dimensional image of the micro X-ray images of the packed quartz sand medium, and a network structure extracted from the selected red square area

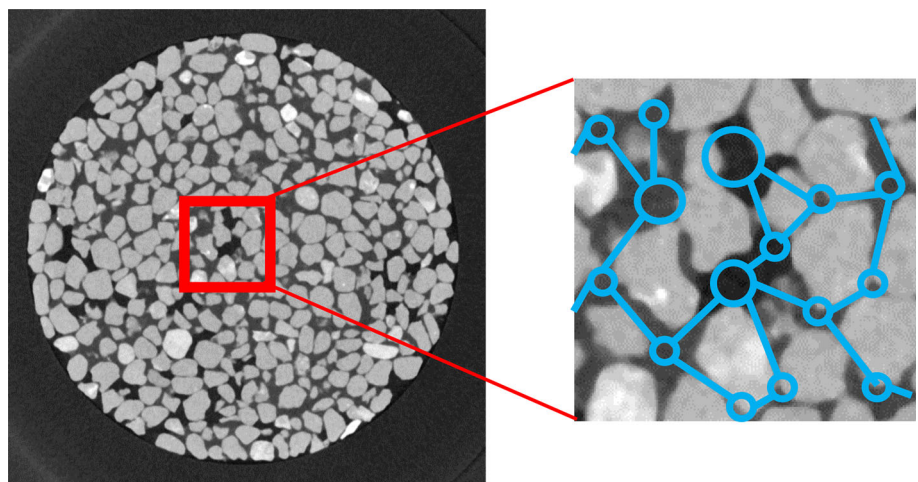


Fig. 5 Distributions of **a** pore radius and **b** throat radius for the packed quartz sand. The dashed lines are the gamma distributions with the fitted parameters a and b

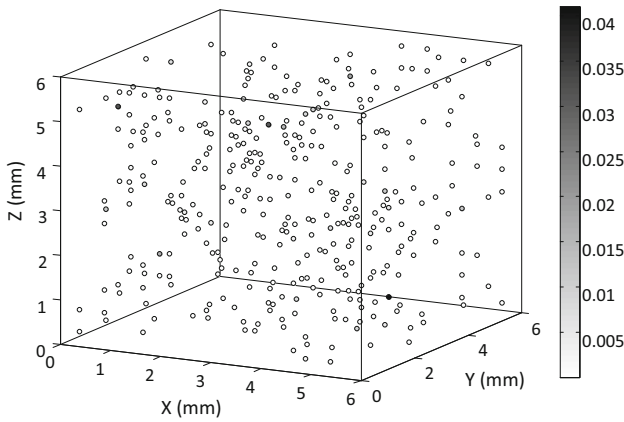
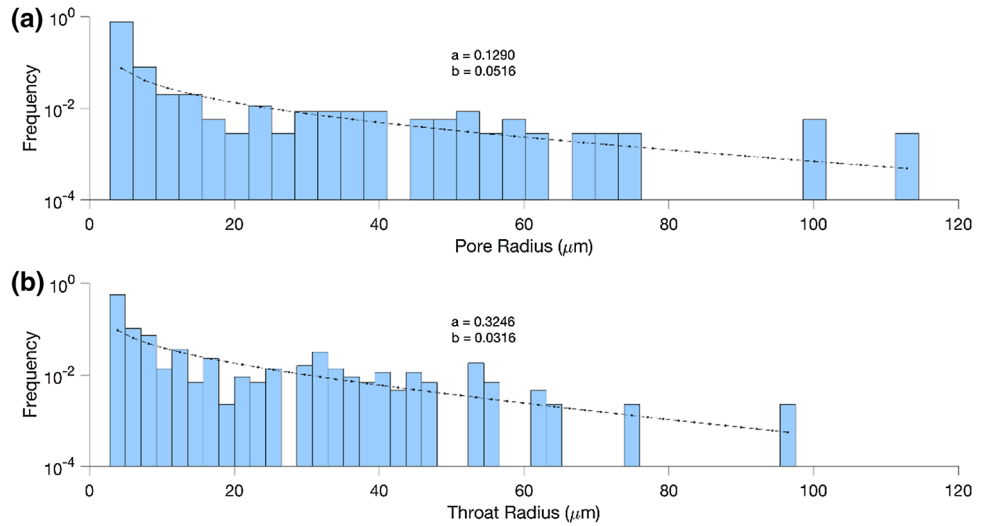


Fig. 6 Simulation of the pore size and location of the network by using the Monte Carlo method

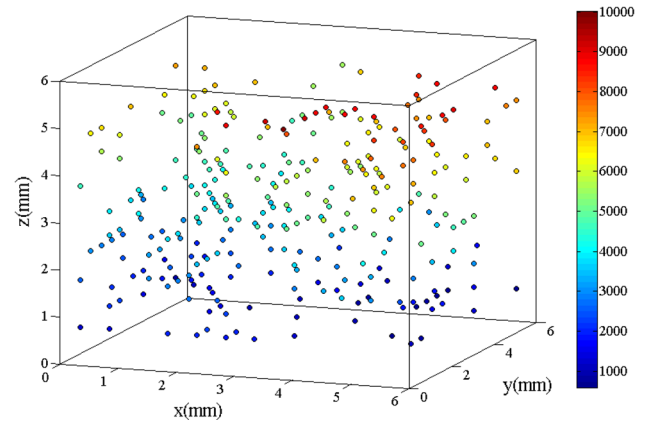


Fig. 8 Water pressures (pa) of the pore bodies

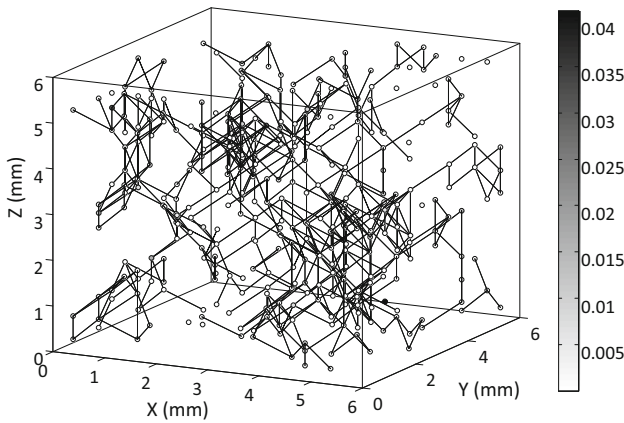


Fig. 7 Simulation of a pore network by using the Monte Carlo method

(303 pressure variables, $x_{p,r1}$, for the inner pores and 443 flow variables, $x_{f,r1,r2}$, for the pore throats) and 746 equations [303 mass balance equations in Eq. (9) and 443

Poiseuille’s equations in Eq. (10)]. By solving the system of equations, we can determine the pore pressure and throat flow rate. See Fig. 8 for the distribution of the pore

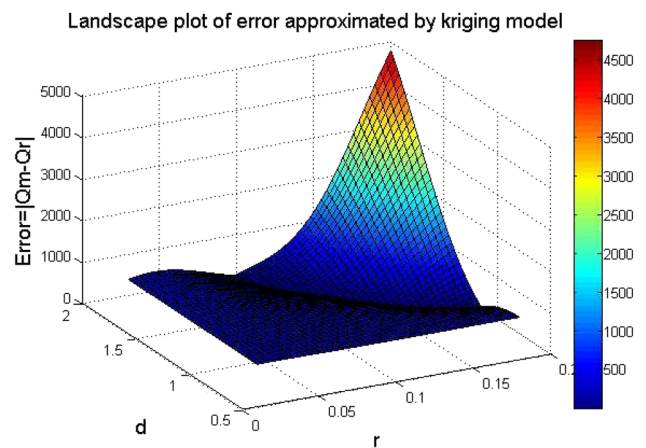


Fig. 9 Relationship between the simulation error, the throat radius, and the connecting distance

pressure. We also calculated the total flow rate, Q_m , which is the summation of flow rates in all pore throats of the pore structure.

By adjusting the value of the arc radius and the connecting distance, we were able to plot the relationship between the simulation error, the throat radius, and the connecting distance. Figure 9 shows the deviation (simulation error) between the modeled flow rates of the pore networks (based on different values of r and d) from the measured total flow rates. The pore throat radius and connecting distance were significant factors for the porous media flow simulation; a sensitivity analysis of the throat radius and connecting distance was conducted. The results showed that a larger radius and a shorter connecting distance increased the total flow rate in the model. In Fig. 10, the total flow rate increased as we increased the throat radius under the same pressure gradient since the viscous pressure drop decreased as the arc radius increased on the basis of Poiseuille’s law. When the connecting distance was increased, each pore connected to more pores, and the connectivity of the pore network also increased. As a consequence, the hydraulic conductivity increased. Therefore, on the basis of Darcy’s law, the total flow rate increased as we increased the connecting distance, as shown in Fig. 11.

Furthermore, the computational efficiency of the newly developed KASA algorithm and that of the original simulated annealing algorithm were compared. An NET-PFS error minimization problem is formulated as follows. Equation (10) computes objective function of simulation error between estimated flow rate, Q_m , and true flow rate, Q_r . The optimization model seeks minimal error by adjusting arc radius of r and connecting distance of d ; the objective function is subject to constraints of NET-PFS model.

$$\text{MIN}_{r,d} \left| Q_m(x_{p_{r1}}(r, d), x_{f_{r1,r2}}(r, d)|r, d) - Q_r \right| \quad (10)$$

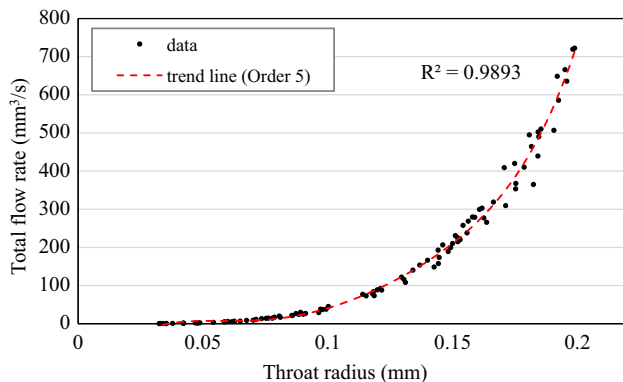


Fig. 10 Sensitivity analysis of the pore throat radius in relation to total flow rate

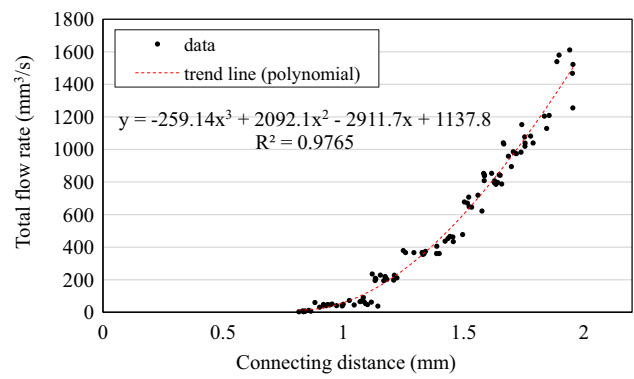


Fig. 11 Sensitivity analysis of the connecting distance in relation to total flow rate

Figure 12 shows that both algorithms converged to optimal solutions. However, KASA can save a significant calculation time by using Kriging approximation instead of running the NET-PFS model. Then, the computation time and cost were reduced because of Kriging approximation. The KASA algorithm was able to provide a higher computational efficiency for the optimization procedures. Suppose the original running time of the model is t_n , and Kriging approximation takes time t_k . For every p iteration of the KASA algorithm, $(p - 1)$ Kriging approximation is performed and the NET-PFS model is run only once. Equation (11) shows that the reduction of the computational time is approximately $(p - 1)(t_n - t_k)$.

$$[(p)(t_n)] - [(p - 1)(t_k) + t_n] = (p - 1)(t_n - t_k) \quad (11)$$

For the NET-PFS simulation of the packed quartz sand medium, Fig. 13 shows that the KASA algorithm reduced the calculation time from 20,000 (s) to 7000 (s). The computational efficiency can be improved further if the simulation model is more complicated. In addition, a sensitivity analysis of the throat radius and connecting distance in terms of computational time was also conducted. Since the throat radius does not change the numbers of control variables and equations of the NET-PFS model, Fig. 14 shows that the sensitivity analysis of the throat radius had less impact on the computational time. However, a larger connecting distance led to greater network complexity, which caused an increase in the computational time for the NET-PFS model, as shown in Fig. 15.

5 Conclusions

In this research, we proposed a framework combining pore network simulation and KASA algorithm to construct the equivalent pore network based on the pore-structure

Fig. 12 Optimization steps of the KASA algorithm and the original simulated annealing algorithm

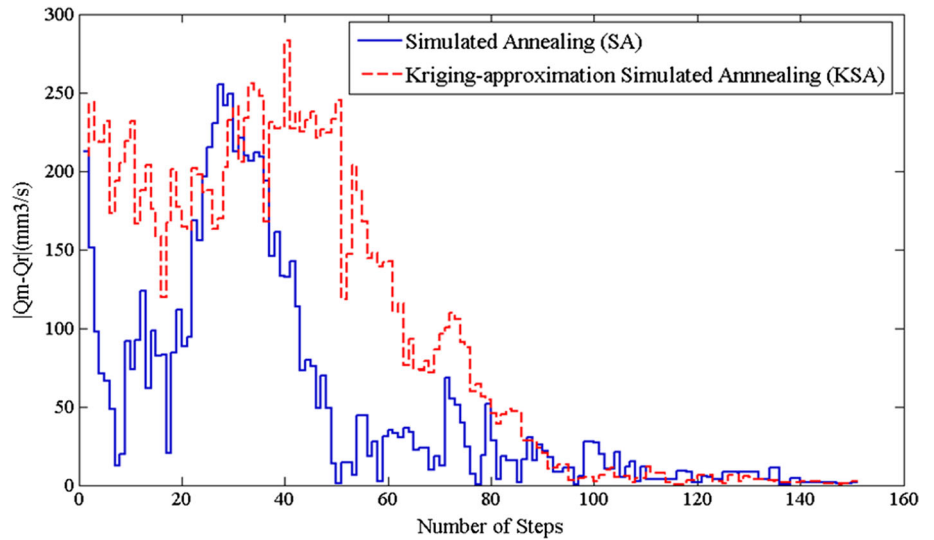


Fig. 13 Calculation time of the KASA algorithm and the original simulated annealing algorithm

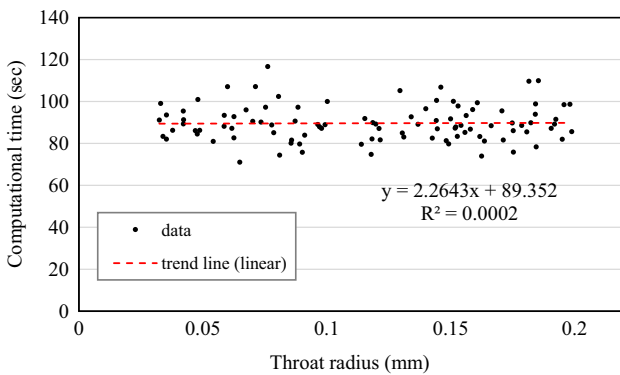
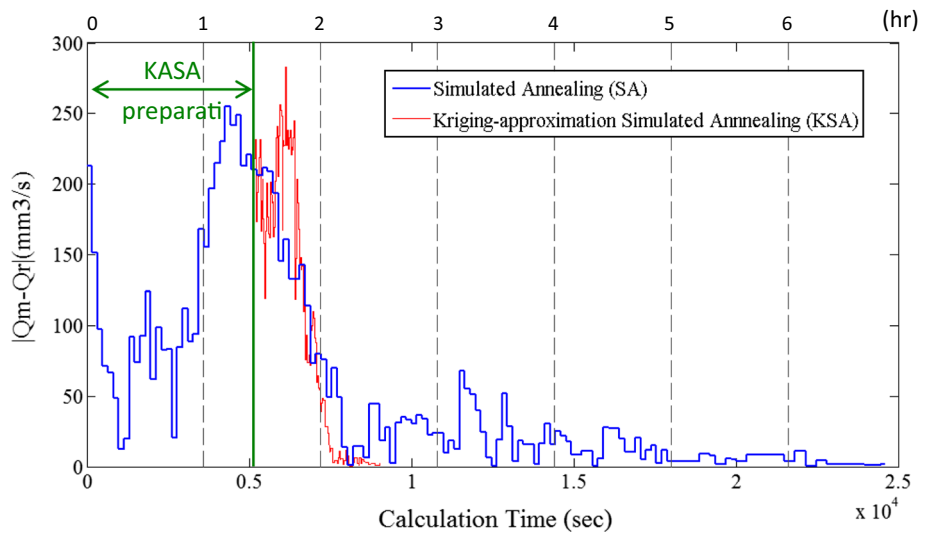


Fig. 14 Relationship between throat radius and computational time ($d = 1.2 \text{ mm}$)

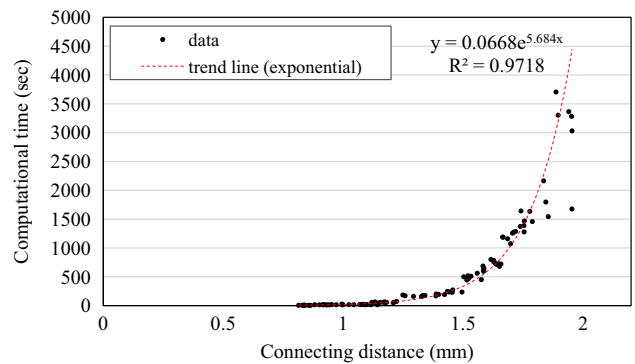


Fig. 15 Relationship between connecting distance and computational time ($r = 0.15 \text{ mm}$)

statistical information from the X-Ray CT image. The case study showed that the proposed method can effectively find a representative pore network for a packed quartz sand

medium. The hydraulic conductivity of the representative pore network was the same as that of the complicated pore structure of the packed quartz sand medium.

In addition, this research developed a new KASA optimization algorithm. The KASA algorithm uses Kriging approximation to avoid the evaluation of the complicated objective function. The proposed KASA algorithm applies Kriging approximation to interpolate the objective value in the solution space rather than to estimate variables in physical space. The advantage of KASA is to reduce the evaluation time of the objective function. Similar to simulated annealing, the KASA algorithm searches for the optimal solution by simulating the cooling process of heated metals. The KASA algorithm is also a heuristic optimization method and can reach the global optimum with a probabilistic technique. Notice that the proposed KASA algorithm interpolates the objective value in the solution space and the uncertainty estimation of Kriging approximation can be determined. The current KASA algorithm does not use uncertainty information in optimum searching procedure. Uncertainty estimation could be incorporated with solutions searching strategy of simulated annealing for future study. In this research, KASA was applied to calibrate the computationally demanding NET-PFS model. The results showed the computational efficiency of the KASA optimization algorithm.

Compared with those of previous studies, the significant contribution of this research includes the development of both the NET-PFS simulation model/framework and an innovative KASA optimization algorithm. Nevertheless, in this study, the control variables were limited to pore throat radius and connecting distance. Future studies should further consider the variations in pore body locations, pore throats, and arc radius. Moreover, in the study, the distributions of the pore volume and arc radius were given. In reality, micro X-ray images of the pore structure might actually be difficult to obtain. The inputs of the optimization framework should be extended to the information that can be obtained with conventional soil analysis experiments without a micro X-ray image, i.e., pore size distribution. Then, the applicability of the optimization framework can be significantly extended. Determined representative pore networks can further be used to estimate the relative permeability, residual phase saturation, and other soil characteristics for single- or multi-phase flows in porous geo-materials.

Acknowledgements The authors thank the editors and anonymous referees for thoughtful comments and suggestions. The authors are responsible for the opinions and comments. This research was funded by the Taiwanese Ministry of Science and Technology (MOST-105-2627-M-002-037; 105T612C502; MOST 106-2628-M-002-009-MY3) and National Taiwan University (NTU-CCP-106R891007; NTU-CC-107L892607).

References

- Al-Kharusi AS, Blunt MJ (2007) Network extraction from sandstone and carbonate pore space images. *J Pet Sci Eng* 56(4):219–231
- Bakke S, Øren PE (1997) 3-D pore-scale modelling of sandstones and flow simulations in the pore networks. *Spe J* 2(02):136–149
- Bechler A, Romary T, Jeanne N, Desnoyers Y (2013) Geostatistical sampling optimization of contaminated facilities. *Stoch Environ Res Risk Assess* 27:1967
- Blunt MJ, Jackson MD, Piri M, Valvatne PH (2002) Detailed physics, predictive capabilities and macroscopic consequences for pore-network models of multiphase flow. *Adv Water Resour* 25(8):1069–1089
- Blunt MJ, Bijeljic B, Dong H, Gharbi O, Iglauer S, Mostaghimi P, Paluszny A, Pentland C (2013) Pore-scale imaging and modelling. *Adv Water Resour* 51:197–216
- Bryant S, Blunt M (1992) Prediction of relative permeability in simple porous media. *Phy Rev A* 46(4):2004
- Bryant SL, King PR, Mellor DW (1993a) Network model evaluation of permeability and spatial correlation in a real random sphere packing. *Transp Porous Media* 11(1):53–70
- Bryant SL, Mellor DW, Cade CA (1993b) Physically representative network models of transport in porous media. *AIChE J* 39(3):387–396
- Cao K, Ye X (2013) Coarse-grained parallel genetic algorithm applied to a vector based land use allocation optimization problem: the case study of Tongzhou Newtown, Beijing, China. *Stoch Environ Res Risk Assess* 27:1133
- Cieniawski SE, Eheart JW, Ranjithan S (1995) Using genetic algorithms to solve a multiobjective groundwater monitoring problem. *Water Resour Res* 31(2):399–409
- Coelho D, Thovert JF, Adler PM (1997) Geometrical and transport properties of random packings of spheres and aspherical particles. *Phy Rev E* 55(2):1959
- de Lavenne A, Skøien JO, Cudennec C, Curie F, Moatar F (2016) Transferring measured discharge time series: large-scale comparison of top-Kriging to geomorphology-based inverse modeling. *Water Resour Res* 52(7):5555–5576
- Dong H, Blunt MJ (2009) Pore-network extraction from micro-computerized-tomography images. *Phy Rev E* 80(3):036307
- Dougherty DE, Marryott RA (1991) Optimal groundwater management: 1. Simulated annealing. *Water Resour Res* 27(10):2493–2508
- Dullien FA (2012) *Porous media: fluid transport and pore structure*. Academic Press
- Jiang X, Lu W, Na J, Hou Z, Wang Y, Chi B (2018) A stochastic optimization model based on adaptive feedback correction process and surrogate model uncertainty for DNAPL-contaminated groundwater remediation design. *Stoch Environ Res Risk Assess* 32:3195. <https://doi.org/10.1007/s00477-018-1559-4>
- Keehm Y, Mukerji T, Nur A (2004) Permeability prediction from thin sections: 3D reconstruction and Lattice-Boltzmann flow simulation. *Geophys Res Lett* 31:L04606. <https://doi.org/10.1029/2003GL018761>
- Ketcham RA, Carlson WD (2001) Acquisition, optimization and interpretation of X-ray computed tomographic imagery: applications to the geosciences. *Comput Geosci* 27(4):381–400
- Laaha G, Skøien JO, Blöschl G (2014) Spatial prediction on river networks: comparison of top-Kriging with regional regression. *Hydrol Process* 28(2):315–324
- Lamorski K (2016) X-ray computational tomography facility. Institute of Agrophysics PAS. <http://tomography.ipan.lublin.pl>. Accessed 18 Sept 2016

- Lerdahl TR, Oren PE, Bakke S (2000) A predictive network model for three-phase flow in porous media. In: SPE/DOE improved oil recovery symposium. Society of Petroleum Engineers
- Marryott RA, Dougherty DE, Stollar RL (1993) Optimal groundwater management: 2. Application of simulated annealing to a field-scale contamination site. *Water Resour Res* 29(4):847–860
- Miao X, Gerke KM, Sizonenko TO (2017) A new way to parameterize hydraulic conductances of pore elements: A step towards creating pore-networks without pore shape simplifications. *Adv Water Resour* 105:162–172
- Okabe H, Blunt MJ (2004) Prediction of permeability for porous media reconstructed using multiple-point statistics. *Phys Rev E* 70(6):066135
- Oliver MA, Webster R (1990) Kriging: a method of interpolation for geographical information systems. *Int J Geogr Inf Sci* 4(3):313–332
- Øren PE, Bakke S (2002) Process based reconstruction of sandstones and prediction of transport properties. *Transp Porous Media* 46(2–3):311–343
- Oren P-E, Bakke S, Arntzen OJ (1998) Extending predictive capabilities to network models. *SPE J* 3(04):324–336
- Pilotti M (2000) Reconstruction of clastic porous media. *Transp Porous Media* 41(3):359–364
- Piri M, Blunt MJ (2005) Three-dimensional mixed-wet random pore-scale network modeling of two- and three-phase flow in porous media. I. Model description. *Phys Rev E* 71(2):026301
- Raeini AQ, Bijeljic B, Blunt MJ (2015) Modelling capillary trapping using finite-volume simulation of two-phase flow directly on micro-CT images. *Adv Water Resour* 83:102–110
- Steeffel CI, Beckingham LE, Landrot G (2015) Micro-continuum approaches for modeling pore-scale geochemical processes. *Rev Mineral Geochem* 80:217–246
- Verdin A, Rajagopalan B, Kleiber W, Funk C (2015) A Bayesian Kriging approach for blending satellite and ground precipitation observations. *Water Resour Res* 51(2):908–921
- Xiong Q, Baychev TG, Jivkov AP (2016) Review of pore network modelling of porous media: experimental characterisations, network constructions and applications to reactive transport. *J Contam Hydrol* 192:101–117
- Yeh WWG (1986) Review of parameter identification procedures in groundwater hydrology: the inverse problem. *Water Resour Res* 22(2):95–108
- Yeong C, Torquato S (1998) Reconstructing random media. *Phys Rev E* 57(1):495

Publisher's Note Springer Nature remains neutral with regard to jurisdictional claims in published maps and institutional affiliations.